Nanoscale

Accepted Manuscript

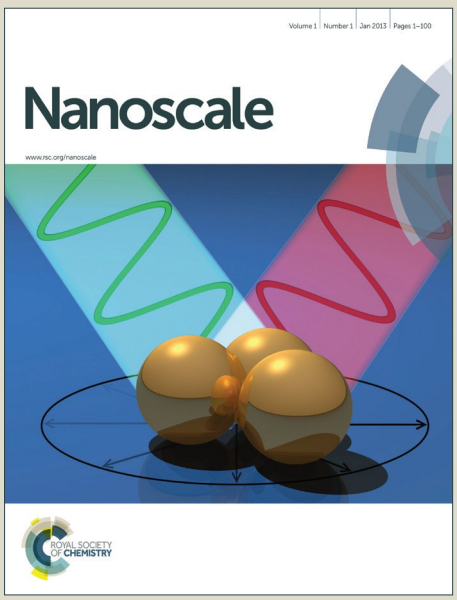

ROYAL SOCIETY OF CHEMISTRY

www.rsc.org/nanoscale

Nanoscale

RSCPublishing

PAPER

Nano-Structural Characteristics of Carbon Nanotube-Polymer Composite Films for High-Amplitude Optoacoustic Generation

DOI: 10.1039/x0xx00000x

Hyoung Won Baac,[a] Jong G. Ok,[b] Taehwa Lee,[c] and L. Jay Guo*[cd]

We demonstrate nano-structural characteristics of carbon nanotube (CNT)-polydimethylsiloxane (PDMS) composite films that can be used as highly efficient and robust ultrasound transmitters for diagnostic and therapeutic applications. An inherent architecture of the nano-composite provides unique thermal, optical, and mechanical properties that are accommodated not just for efficient energy conversion but also extraordinary robustness against pulsed laser ablation. First, we explain thermo-acoustic transfer mechanism within the nano-composite. CNT morphologies are examined to determine a suitable arrangement for heat transfer to the surrounding PDMS. Next, we introduce an approach to enhance optical extinction of the composite films, which uses shadowed deposition of a thin Au layer through an as-grown CNT network. Finally, the transmitter robustness is quantified in terms of laser-induced damage threshold. This reveals that CNT-PDMS films can withstand an order-of-magnitude higher optical fluence (and extinction) than that of a Cr film used as a reference. Such robustness is crucial to increase the maximum-available optical energy for optoacoustic excitation and pressure generation. All of these structure-originated characteristics manifest CNT-PDMS composite films as excellent optoacoustic transmitters for high-amplitude and high-frequency ultrasound generation.

Received 00th January 2015,
Accepted 00th January 2015

DOI: 10.1039/x0xx00000x

www.rsc.org/nanoscale

1. Introduction

Piezoelectric transducers are currently the dominating platform to generate biomedical ultrasound for diagnostic and therapeutic applications. As an emerging technology, optical generation of ultrasound has been actively investigated over decades to develop transmitters, employing pulsed laser irradiation onto optical absorbers [1–5]. This enables non-resonant generation of ultrasound pulses with high-frequency and broadband spectra (*e.g.* several tens of MHz for a laser pulse width of 5–10 ns) and non-contact definition of a transmitter element by a laser spot [2,3]. From optoacoustic transmitters, high-frequency components up to 57 MHz have been produced and used for ultrasound imaging of microscale features [5]. Recently, focal transmitters with a 15-MHz center frequency have been demonstrated for laser-generated focused ultrasound (LGFU) that enables micro-ultrasonic treatment for high-precision therapy [6–8], controlled single-bubble generation [9], and micro-droplet ejection [10]. However, such utilization of high-frequency ultrasound has been limited to proximity applications (*e.g.* <1 cm) due to severe acoustic attenuation with an increasing distance of propagation in water and tissues (*e.g.* attenuation coefficient in water: 2.2×10^{-3} dB cm^{-1} MHz^{-2}). A stronger pressure output from the transmitters would greatly extend the use of high-frequency components over a deeper region for high-resolution ultrasonic imaging or precision therapy.

Thin-film transmitters for optoacoustic generation were introduced using metallic coatings [1] or microscale dye absorbers [11,12]. However, it has been challenging to achieve both high-pressure amplitudes and high-frequency spectra in a single transmitter. The early use of microscale absorbers was intended to increase optical absorption (up to 100%), and usually prepared as a mixture with polymer for thin-film formation. The inclusion of microscale particles or powders resulting in a thick absorption layer (>a few tens of μm) significantly increases internal acoustic attenuation and ultrasonic pulse broadening through the film. These structures were not desirable for high-frequency ultrasound generation, which is one of the major motivations to use the optoacoustic approach. Spatial non-uniformity of the absorbing elements was an additional issue that causes uneven generation of high-frequency acoustic waves over the film. These shortcomings motivated more sophisticated transmitters adopting a thinner and

[a] School of Electronic and Electrical Engineering, Sungkyunkwan University, Suwon 440-746, Republic of Korea.
[b] Department of Mechanical and Automotive Engineering, Seoul National University of Science and Technology, Seoul 139-743, Republic of Korea.
[c] Department of Mechanical Engineering, University of Michigan, Ann Arbor, MI 48109, USA.
[d] Department of Electrical Engineering and Computer Science, University of Michigan, Ann Arbor, MI 48109, USA.

more uniform absorption layer, still providing reasonably high optical absorption (*e.g.* >70 %) [13–18]. This requirement was satisfied by using nano-structured transmitters such as 2-D Au nano-particle arrays [13], CNTs [14,15], carbon nano-fibers [16], reduced graphene oxides [17], and 1-D photonic crystals [18].

Especially, optoacoustic transmitters using CNT-PDMS (polydimethylsiloxane) composite films could produce powerful ultrasonic outputs over a high-frequency broad bandwidth from dc to ~80 MHz (6-dB roll off) [14]. An optoacoustic conversion efficiency was 1~2 orders-of-magnitudes higher than that of a reference metal film (*e.g.* Cr) [14,19,20]. Furthermore, CNT-PDMS composite films could be fabricated on various geometries: for example, a spherical lens surface (6- and 12-mm diameter) for high-pressure focal therapy [6] and an optical fiber as a miniature transmitter (105-μm diameter) [15]. The focal transmitter produced a bipolar ultrasonic pulse with peak amplitudes reaching tens of MPa at a tight spot of ~75 μm, leading to strong local disruption via shock and cavitation effects [6,7]. This opened up new possibilities of micro-ultrasonic therapy and surgery capable of targeting even a few cells [7,8].

Although the adoption of nano-structured films has attracted broad multi-disciplinary interests to achieve high optical absorption in a thin film [13–18,21], there has been serious lack of understanding about structural benefits from a nanoscopic origin that can be associated with thermal energy conversion and mechanical robustness against laser-induced ablation. Particularly, the robustness, which has been largely overlooked so far, is important because an output pressure can be increased with input pulse laser energy as long as the structure is durable. The upper limit of the pulse energy would be readily determined by the laser damage threshold where physical ablation of a light-absorbing material occurs. The robustness varies greatly according to the structural detail of thin-film transmitters. While the optical absorption of recent advanced transmitters varies mostly within ±30%, variation in the upper limit of the laser energy available for pressure generation can be more than several folds.

In this work, we demonstrate nano-structural characteristics of CNT-PDMS composite films. This explains that the internal structure of the nano-composite film is inherently suitable for efficient optoacoustic conversion and high-energy pulsed laser excitation without physical damage. We first explain the thermo-elastic energy conversion process within the CNT-PDMS film that is attributed to rapid heat transfer from CNTs to the surrounding PDMS, and examine the composite morphology that allows efficient heat transfer. Then, we introduce Au-hybridized CNT transmitters by depositing a thin Au layer over as-grown CNT films. Finally, the extraordinary robustness of the nano-composite is quantified by measuring the laser damage threshold. This confirms that CNT-PDMS composite films have 10-fold higher damage threshold energy fluence than that of a Cr film used as a reference (and also for maximum-available laser energy fluence for pressure generation). All of these characteristics and modification utilizing the nano-structural arrangement are advantageous for high-amplitude and high-frequency ultrasound generation.

2. Results and discussion

2.1 Thermoacoustic characteristics

Rapid heat transfer is one of the major physical characteristics of CNTs and nanoscale particles [22]. The characteristic heat transition time (τ_{HD}), where the excess temperature of a heated element drops to one half of an initial value, is estimated as 0.4 ns for a single CNT strand (25-nm diameter) surrounded by an elastomeric polymer (here, PDMS) where $\tau_{HD} = d^2/16\chi$ for a cylindrical structure with the diameter d and the thermal diffusivity of the surrounding medium χ [23]. Therefore, the heat transition time is much shorter than laser pulse widths typically used for optoacoustic excitation (τ_L = 5−10 ns). This implies that, during pulsed laser irradiation, the optically deposited thermal energy is not confined within the absorber. This is in contrast from those of microscale light-absorbing contrast agents used for optoacoustic imaging. In that case, the heat is strongly confined within the microscale absorbers and used for rapid pressure generation before heat diffusion; and the surrounding medium makes relatively less or negligible contribution to the optoacoustic generation process.

Such extremely fast heat transition in nanoscale absorbers to the surrounding environment can be utilized for more efficient optoacoustic generation. A remnant heat within a nano-particle after the temporal laser pulse of τ_L can be estimated as [24],

$$\Delta T = \frac{F\mu}{\rho_s c_{ps}} \times \frac{\tau_{HD}}{\tau_L} \times \left[1 - exp\left(-\frac{\tau_L}{\tau_{HD}} \right) \right] \quad (1)$$

where ΔT, F, μ, ρ_s, and c_{ps} are temperature increase, laser energy fluence, absorption coefficient, density, and specific heat capacity, respectively. Particularly, we can define the energy fraction (η) still available for heating the nano-particle after τ_L [23]:

$$\eta = \frac{\tau_{HD}}{\tau_L} \times \left[1 - exp\left(-\frac{\tau_L}{\tau_{HD}} \right) \right]. \quad (2)$$

Figure 1 shows the energy fraction η as a function of the cylinder diameter d (for τ_L = 6 ns). In the regime of $\tau_{HD} << \tau_L$, nanoscale absorbers transfer most of the thermal energy to the surrounding medium, *e.g.* η = 6% for 25-nm thick CNTs. Comparatively, η quickly approaches to 99% with 1-μm thick absorbers, strongly confining the heat where $\tau_{HD} >> \tau_L$. Due to the rapid and efficient heat transition from CNTs, the generation of thermoacoustic pressure is dominated by the surrounding PDMS that receives most of the transferred thermal energy (~94%). Thus, the thermal expansion occurs over the cylindrical volume of PDMS surrounding a single CNT strand with a characteristic depth of thermal penetration, *i.e.* tens of nm for nanoseconds pulse width. This suggests that

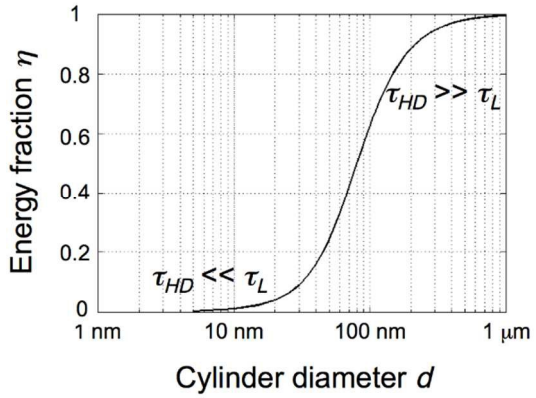

Fig. 1 A fraction of thermal energy within a cylindrical absorber after laser pulse duration (τ_L = 6 ns).

our CNT-based composite structure efficiently utilizes high thermal expansion of the elastomeric PDMS (thermal expansion coefficient ~ 0.92×10^{-3} K^{-1}; Grüneisen coefficient ~ 0.72) while other microscale absorbers generate an output pressure via their own thermal expansion process with significantly lower coefficients than that of PDMS. Moreover, PDMS readily allows acoustic impedance matching with water. At a glance, the CNT-PDMS mixture is similar with piezo-ceramic composites, widely used for piezoelectric transducers, consisting of ceramic elements embedded in a polymer matrix [25]. However, in the CNT-PDMS composite, the PDMS works as an essential thermoelastic source that dominates the pressure generation, receiving most of the thermal energy available from the CNTs.

For a transmitter containing CNT absorbers, we can estimate the output pressure by the following analysis. Here, a pressure pulse is generated by the portion of the CNT-driven thermal energy used for volume expansion of the surrounding PDMS, which corresponds to $1-\eta$. Therefore, for a long pulse excitation regime (since the laser pulse width is longer than the acoustic transit time across the depth of optical penetration) and a Gaussian laser pulse [26], we can represent a peak pressure amplitude P approximately as

$$P = \frac{\Gamma}{c}\frac{F}{\tau_L}\times(1-\eta)\times A \qquad (3)$$

where Γ, c, and A are Grüneisen coefficient, sound speed and optical absorption. The absorption is given as $1-T-R-S$ for T: transmittance, R: reflectance, and S: scattering. The above model intuitively explains that the CNT-PDMS transmitter takes full advantages in each physical factors: high Grüneisen coefficient (Γ) of PDMS, high optical absorption (A) of CNT, and the efficient heat transfer process ($1-\eta$) originated from the nanoscale dimension absorber. Furthermore, it is confirmed in sections 2.4 and 2.5 that the transmitter can withstand high-energy optical fluence (F) without laser ablation, so that an upper limit of the optical energy available for pressure generation can be far more than those of other transmitters.

2.2 Morphological characteristics

2.2.1 Nano-composite morphology for efficient heat transition

We prepared as-grown CNT films (see experimental section) and deposited a thin Au layer (20~30 nm) to enhance optical absorption by using an electron-beam evaporation process. Then, the Au-coated CNT films were spin-coated with PDMS for forming the composite film.

We examined CNT-PDMS composite transmitters by scanning electron microscopy (SEM) to investigate how the morphology of CNTs allows the efficient heat transfer to PDMS. The first row in Fig. 2 shows top views of the prepared CNTs with different areal density after Au deposition. In the sparse CNT network (Fig. 2(a)), the CNTs remain tangled due to the small areal density and do not entirely conceal the substrate surface, resulting in low optical absorption, while the areal coverage increases with the growth time of CNT in the chemical vapor deposition chamber (Figs. 2(b) and 2(c)). As shown in the side views (second row), the CNT morphology depends on their areal density. With longer growth time, the initially entangled CNTs (Fig. 2(d) and 2(e)) grow to vertically

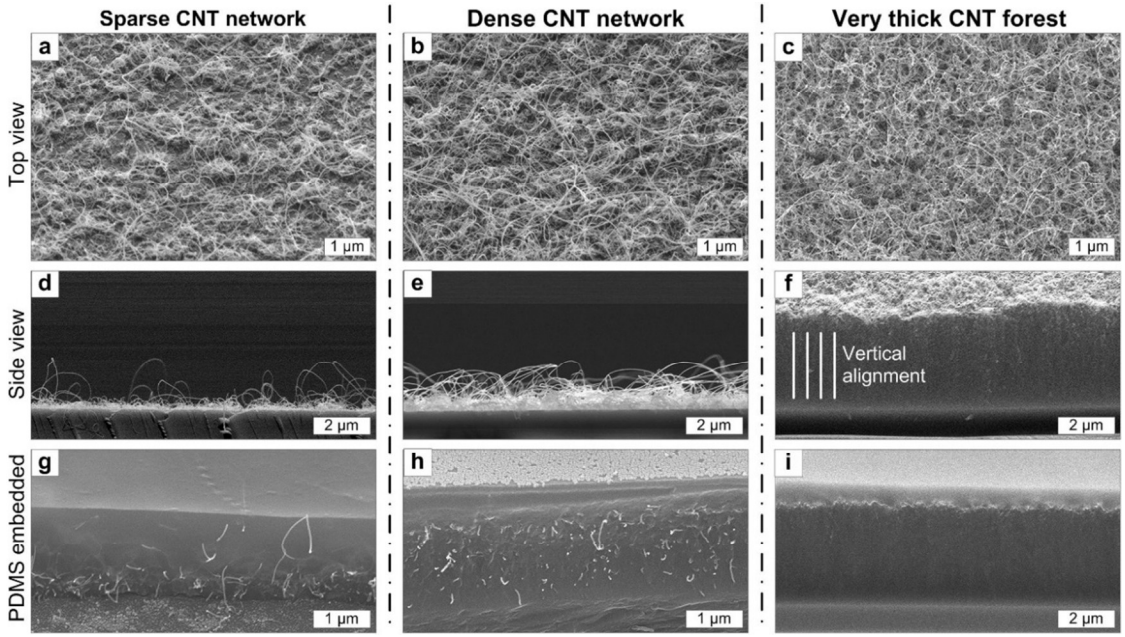

Fig. 2 SEM photographs of the CNT films that are prepared in different areal densities. Before PDMS embedment, a 20-nm thick Au layer was deposited on all of the CNT films: (First row) Top views for (a) sparse, (b) dense CNT networks, and (c) thick CNT forest. The substrate coverage increases with the areal density of CNT; (Second row) Side views of each CNT films on the fused silica substrate in (d)~(f). The self-aligned structure in (f) is due to a crowding effect, forming the Au layer deposited mostly on top of them; (Third row) Structures after spin-coating with PDMS in (g)~(i). Note that the PDMS was completely infiltrated down to the substrate surface for the relatively low-density films as shown in (g) and (h), while the polymer did not penetrate through the CNT forest in (i).

aligned 'forest' due to a crowding effect among high-density CNT strands (Fig. 2(f)) [27]. However, the thick CNT forest formed by the dense and long strands prevents PDMS from being infiltrated (Fig. 2(i)). In this case, the individual CNT has a physical contact with PDMS only at the top end, leading to poor heat transition from CNT to PDMS. Fig. 2(g) and (h) show well-mixed composites in which the CNTs are successfully embedded in the PDMS. We note that the PDMS is completely infiltrated through the CNT network, reaching to the underlying substrate surface. This provided an added benefit of greatly improved adhesion with the substrate than just the CNT forest. Such 3-D embedment ensures better thermal transition from CNT to PDMS. The individual CNT is almost completely enclosed except the stem at the bottom end. Furthermore, the composite films shown in Fig. 2(g) and 2(h) have structural robustness. The infiltrated PDMS, as thermally cured at 100 °C, forms strong adhesion with the substrate (fused silica). In contrast, the PDMS cannot penetrate into the CNT forest in Fig. 2(f), therefore leaving as-grown CNTs on the substrate. Without the PDMS infiltration, the bottom interface of CNT strands with the substrate was not robust. The CNTs were easily ablated from the substrate by optical irradiation with low-energy laser pulses (<50 mJ/cm^2/pulse). This implies that the PDMS linking with the substrate is necessary for mechanical robustness and thus for high-energy optical absorption without laser-induced thermal breakage.

2.2.2 Au-deposited CNT film structure

While the tall and aligned CNT forest can be easily prepared to obtain high optical absorption up to 100% [21,28,29], a well-mixed composite with PDMS is not formed with the forest. Rather, the CNT network with larger spacing among the CNT strands is preferred for PDMS infiltration and 3-D heat transfer from CNTs. However, such less dense structure leads to lower optical absorption than the CNTs in the forest morphology. For optoacoustic transmitter applications, we could reproducibly grow non-forest-type CNT films with optical absorption up to ~80%.

In order to improve the optical absorption for optoacoustic excitation, we utilized the lateral spacing among the CNT strands to deposit additional light-absorbing elements (Fig. 3(a)). We deposited the Au (20~30 nm in thickness) over the as-grown CNTs by an electron-beam evaporation process. Figures 3(b) and 3(c) compare two nano-composite films with and without the Au deposition. Both CNT films were initially grown under the identical condition. After the Au deposition, the composite films were partially peeled off to allow a closer look at the substrate surfaces underneath. Figure 3(b) reveals an Au layer in the form of random nano-clusters on the underlying substrate surface, while the substrate is obviously clean for the pristine CNT-PDMS composite shown in Fig. 3(c). As the Au deposition process was less shadowed by the sparse CNTs, the substrate-bound Au islands were formed with a wide surface coverage.

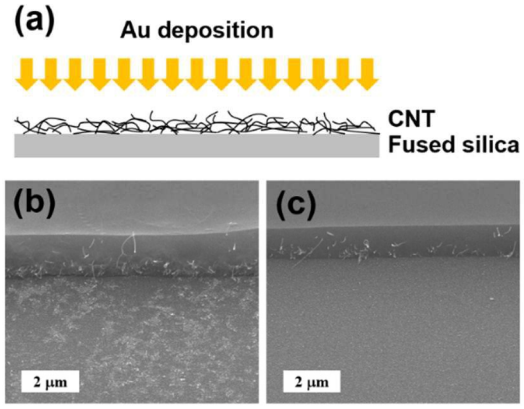

Fig. 3 Au deposition to enhance optical extinction. (a) A schematic of the shadowed deposition process through the as-grown CNT network. (b) After PDMS coating, a part of the CNT-PDMS composite film was peeled off (the image was zoomed out from Fig. 2(g)). The bottom part of the figure shows the substrate-bound Au islands (30-nm thickness in this example) that work as additional elements for enhanced optical extinction. (c) A reference composite film without the Au deposition.

Here, the Au was used to form nano- or micro-clusters on the substrate to increase optical absorption at the pulsed laser wavelength (532 nm). The Au is also preferred due to its high stability. Other metals may be considered if they can contribute to optical absorption over an excitation wavelength.

2.3 Enhanced optical extinction and optoacoustic pressure by Au deposition

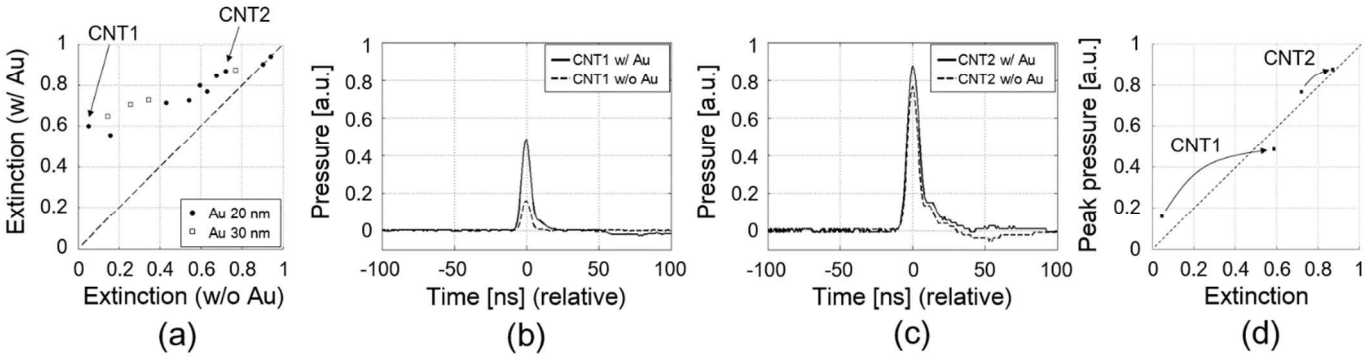

Fig. 4 Enhancement of optical extinction and optoacoustic pressure: (a) Optical extinction of various CNT films without and with Au deposition (horizontal and vertical axis, respectively); (b) and (c) Pressure waveforms from CNT1 and CNT2 films after composite formation with PDMS. Each figure compares two waveforms: one with Au deposition (solid) and the other without Au deposition (dashed); (d) Peak pressure amplitudes in (b) and (c) are shown versus optical extinction. The dotted line is set only for visual guidance of linear enhancement.

We measured the optical extinctions of CNT films before and after the Au deposition at 532-nm wavelength (Fig. 4(a)). Various CNT films were prepared with different initial densities and then deposited with the Au layer of 20-nm or 30-nm thickness. The extinction (E) was obtained by $1-T-R$. The oblique line in Fig. 4(a) means no enhancement in the extinction before and after Au deposition. The enhancement effect is shown as a gap between each data point and the oblique line.

The comparison of various films reveals pronounced extinction enhancement for those CNT films initially grown with low areal density, while the dense CNT films have negligible enhancement by the Au deposition. This is because the Au deposition leads to a greater amount of surface-bound Au nano-clusters for the lower-density CNT films than those of the higher-density films. The Au clusters at the bottom of the CNTs can either absorb or scatter the incident light, which significantly helps the optical absorption process by the CNTs. The 30-nm deposited films exhibited slightly greater enhancement than those with the 20-nm deposited ones, due to higher absorption of a thicker Au layer formed at the substrate surface.

It is noteworthy that the extinction increment for the initially low-density CNT films (ΔE = 0.3~0.55) was even larger than the extinction available from a pure Au layer with 20- or 30-nm thickness. For example, the optical extinction of a 20-nm thick continuous Au film was just 0.28 (T = 0.54, R = 0.18). Here, such distinctive enhancement (ΔE > 0.28) can be attributed to the significantly enhanced optical scattering by the shadow-deposited Au layer in the form of nano or microscale islands rather than a 1-D planar film. Forward-scattered light from the Au islands at the substrate is then absorbed by CNT strands filled over several μm thickness. Also, back-scattered light from the Au clusters on top of the CNTs facilitates optical absorption by the substrate-bound Au as well as the CNTs underneath. Evidently, our approach provides an effective route to increase the optical extinction of sparsely grown CNT films up to 0.7~0.8 by a single-step Au deposition process.

The enhancement behavior observed in the optical extinction was also confirmed in the optoacoustic pressure (Fig. 4(b) and 4(c)). An Nd:YAG pulsed laser beam (532-nm wavelength, 6-ns pulse width, Surelite I-20, Continuum, Santa Clara, CA) was used for optoacoustic generation. We compared two films containing CNTs with different optical extinctions: CNT1 (E = 0.05 before Au deposition and E = 0.60 after 20-nm Au deposition) and CNT2 (E = 0.72 before Au deposition and E = 0.87 after 20-nm Au deposition). In the CNT1, the peak pressure was enhanced up to 3.2 fold after the Au deposition, while the CNT2 had just 14% improvement by the same 20-nm thick Au deposition. All films were irradiated with an identical laser fluence (<20 mJ/cm^2) in a non-ablative regime. Figure 4(d) shows that the pressure enhancement is approximately linear along with the optical extinction at this low-energy excitation regime.

2.4 Mechanical robustness for high-energy optical excitation

For CNT-PDMS composite transmitters with a given absorption coefficient, a higher incident laser energy can lead to a stronger output pressure. However, pulsed laser irradiation should not cause physical damage to the transmitter for reproducible operation. An upper energy limit for the pulsed laser is determined by the laser damage threshold. In this sense, a higher damage threshold means a higher pressure ultimately attainable from transmitters.

We quantified the robustness of CNT-PDMS composite films by measuring the laser damage threshold. The same pulsed laser beam with 532-nm wavelength was expanded and irradiated onto a film through a circular aperture with 1-mm diameter. Under the identical irradiation condition, we compared laser ablation processes of

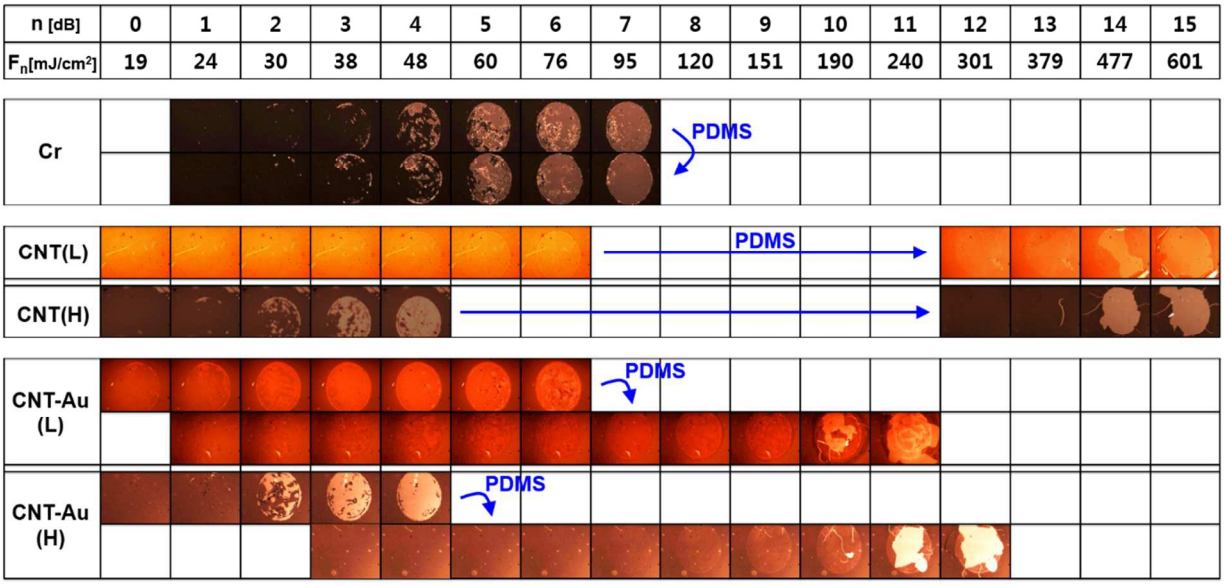

Fig. 5 Photographic demonstration of laser-induced ablation on Cr and CNT films under pulsed laser irradiation (τ_L = 6 ns) through an aperture with 1-mm diameter. A given laser fluence (F_n) is denoted at the second row, and the irradiated film images shown below. Laser ablation of the Cr film starts to appear with the fluence of 30~38 mJ/cm^2 for both cases before (upper row) and after PDMS coating (bottom row). The films were fully ablated by the fluence of 95 mJ/cm^2 or higher. For the CNT(L) and the CNT(H), the damage threshold fluences were greatly increased by 10 times after composite formation with PDMS (see photographs on the right side of each row). No ablation was observed for the PDMS-coated CNT(L) and CNT(H) where F_n < 301 mJ/cm^2 (images not shown). For the CNT-Au(L) and the CNT-Au(H), each upper row shows the images without PDMS coating, and each bottom row with PDMS coating.

various films with and without PDMS: Cr film (100-nm thickness) as a reference, CNTs grown with low and high densities (denoted as CNT(L) and CNT(H), respectively), and the same CNTs with Au deposition (denoted as CNT(L)-Au and CNT(H)-Au). The morphologies of CNT(L) and CNT(H) are similar with the sparse and the dense CNT networks shown in Fig. 2(a) and (b). For each film of Cr, CNT(L), CNT(H), CNT(L)-Au, and CNT(H)-Au, the optical extinction at 532-nm wavelength was 0.49, 0.11, 0.58, 0.54, and 0.79, respectively.

Figure 5 shows the microscopic images of the irradiated films. We increased a laser power by a 1-dB step up to 15 dB (denoted by "*n* [dB]" at the top row of Fig. 5). At $n = 0$, an average laser power was 3 mW with 20-Hz pulse repetition. The corresponding pulse energy and fluence were 0.15 mJ and 19 mJ/cm^2/pulse. Then, the energy fluence F_n shown in the second row of Fig. 5 was calculated by $F_n = 10^{n/10} F_0$ where $F_0 = 19$ mJ/cm^2.

For the Cr film, the laser-induced ablation started at $n = 2$~3 dB (*i.e.* 30~38 mJ/cm^2). As expected, the threshold did not change before and after PDMS coating on the Cr layer. This is because the laser ablation occurs at the interface between Cr and substrate, regardless of the PDMS coating. In contrast, the ablation threshold in the CNT films was greatly enhanced after the composite formation with PDMS. As shown in Fig. 5, the ablation threshold energy fluence (F_{th}) was increased by 12.5 folds from $F_{th} \sim 38$ mJ/cm^2 to 477 mJ/cm^2 in the CNT(L), and 16 folds from $F_{th} \sim 30$ mJ/cm^2 to 477 mJ/cm^2 in the CNT(H). The as-grown CNTs without PDMS coating were easily ablated under a relatively low laser fluence of <50 mJ/cm^2. The PDMS-induced improvement in the laser damage threshold and hence the robustness of the nano-composite structure can be attributed to formation of strong adhesion between the PDMS and the silica substrate.

Interestingly, the spatial pattern of ablated films differs for the cases with and without PDMS coating. Without PDMS, the ablated spots within the 1-mm aperture gradually appear for $n = 2$~6 dB for both CNT(L) and CNT(H). For the as-grown CNT films, the CNT strands adhere to the substrate via the catalyst layer only. A light-absorbed CNT strand transfers the heat to the catalyst/substrate interface. Therefore, the films are ablated due to interfacial breakage between the CNT and the substrate. In these CNT films without PDMS, a well-defined circular edge is observed along the circular aperture. This is similar with the Cr film that is ablated by the interfacial delamination from the substrate. However, in the CNT-PDMS composite, a large piece of film was ablated collaterally under the high laser energy ($n \sim 14$ dB) as shown at the right corners of CNT(L) and CNT(H) rows in Fig. 5. In this case, the CNT strands are completely embedded in the PDMS volume matrix. This nano-composite structure not only helps to dissipate the heat in the CNTs to the whole volume of PDMS, but also forms stronger adhesion between the cured PDMS and the substrate surface with a broad contact area. This means that most of the thermal loading generated by the CNTs is released to the surrounding PDMS matrix through the 3-D paths. The heated PDMS delivers the thermal loading to the substrate indirectly and slowly. Direct heat transition from the CNTs to the substrate would be negligible as compared to the 3-D volume path. Therefore, the volume dissipation of CNT-generated heat and the strong PDMS-substrate adhesion enable the composite transmitter to endure much higher laser fluence without damage. In contrast, 1-D absorbers such as Cr film have a wide interfacial contact area with the substrate that works as a direct heat transition path, thus becoming susceptible to thermal damage.

Next, we investigated the Au-deposited CNT composite films. Without PDMS, the damage threshold was similar to those of CNT(L) and CNT(H). However, two-step ablation behaviors were observed when embedded inside the PDMS coating. In the CNT(L)-Au, the laser ablation occurred first at a relatively low fluence near $n_L = 2$~3 dB ($F_{th} = 30$~38 mJ/cm^2) and then abruptly at $n_H = 10$ dB ($F_{th} = 190$ mJ/cm^2). We note that the Au coverage on the substrate surface in the CNT(L)-Au takes a significant portion as Au atoms are deposited through the space unshadowed by the sparsely grown CNTs. Therefore, the substrate-bound Au can cause the low-fluence ablation (n_L). Furthermore, the presence of the substrate-bound Au prevents PDMS from forming adhesion with the substrate. This weakens the overall composite adhesion with the substrate surface, reducing the damage threshold to $F_{th} = 190$ mJ/cm^2 for CNT-Au(L), as compared to 477 mJ/cm^2 for CNT (L). Finally, we also measured the damage threshold of the CNT(H)-Au. This showed similar mixed behaviors but with increased threshold values. In the CNT(H)-Au, the substrate-bound Au has less surface coverage than that of the CNT(L)-Au because the Au deposition is more shadowed by the dense CNT network (initially, $E = 0.58$). Due to the reduced amount of Au on the substrate, the damage threshold was slightly increased by 1~2 dB for both n_L and n_H as compared to the CNT(L)-Au case.

2.5 Maximum-extinction energy fluence

Using the laser damage threshold and the optical extinction, we define the maximum-available optical energy fluence in terms of extinction as $F_{max} = F_{th} \times E$. This provides an upper limit of the optical energy in terms of extinction internally available within the transmitter for pressure generation before ablation occurs. Table 1 summarizes E, F_{th}, and F_{max} of each transmitter. For Cr film, CNT(H), and CNT-Au(L), the optical extinction varies within a narrow range of 0.49~0.58. However, the F_{max} (w/ PDMS) of each transmitter differs greatly from 23.4 up to 276.7 mJ/cm^2, which is more than 10-fold variation. Such a high value of F_{max} in the CNT-PDMS composite guarantees the availability of high-amplitude pressure output from the transmitter.

As confirmed previously, the Au deposition enhances the optical extinction of as-grown CNT films. However, there is a trade-off by the reduction of laser damage threshold due to the inclusion of

Parameter \ Transmitter	Cr	CNT(L)	CNT(H)	CNT-Au(L)	CNT-Au(H)
E	0.49	0.11	0.58	0.54	0.79
F_{th} (w/o PDMS)	48	38	30	24	30
F_{max} (w/o PDMS)	23.4	4.2	17.4	13	23.7
F_{th} (w/ PDMS)	48	477	477	190	240
F_{max} (w/ PDMS)	23.4	52.5	276.7	102.6	189.6

Table 1 Laser damage threshold F_{th} [mJ/cm^2] and maximum-extinction energy fluence F_{max} [mJ/cm^2] for each thin-film transmitter. For all films, the extinction E was measured before PDMS coating.

substrate-interfaced Au. As shown in Table 1, the laser damage threshold F_{th} (w/ PDMS) of CNT(L) and CNT(H) was reduced both from 477 mJ/cm^2 to one half or lower with the Au deposition: 190 and 240 mJ/cm^2 for CNT-Au(L) and CNT-Au(H). Thus, F_{max} (w/ PDMS) was obtained as 102.6 and 189.6 mJ/cm^2, respectively.

The comparison of CNT(H) and CNT-Au(H) shows that the maximum-pressure output available by increasing the incident laser fluence would be higher in the CNT(H) rather than the CNT-Au(H) case, although the CNT(H) has lower optical extinction. For the CNT(L), its optical extinction is just one fifth of CNT-Au(L), but the optical energy fluence up to 52.5 mJ/cm^2 can be used for optoacoustic generation which is one half of CNT-Au(L).

High-amplitude ultrasound applications such as focal therapy (*e.g.* peak pressure: >10 MPa) required pulsed laser irradiation with an order of tens-of-mJ per pulse onto a transmitter, depending on a geometrical design of lens [6]. For an optoacoustic lens with a surface area of ~1 cm^2, this leads to an incident laser fluence (F) of 40~300 mJ/cm^2 that is sufficient to produce focal disruption effects through shock and acoustic cavitation. In this purpose, two composite films shown in Table 1 can be suitably considered: CNT(H) and CNT-Au(H). In a low-energy excitation regime where $F << F_{th}$, an output of the CNT-Au(H) (E = 0.79) would be 36% stronger than that of the CNT(H) (E = 0.58) for an identical laser fluence as we assume the linear proportionality between the optical extinction and the pressure amplitude. However, with increasing the laser fluence, physical damage starts to appear where F approaches F_{th}. Due to the higher F_{th} in the CNT(H), the ultimately attainable maximum pressure would be ~46% higher than that of the CNT-Au(H). This suggests that a transmitter should be chosen according to the laser fluence for optoacoustic excitation and its application. The CNT-Au(H) allows more efficient pressure generation with low-energy optical excitation ($F << F_{th}$), but the CNT(H) is more useful with high-energy excitation when an extreme pressure strength is required (*e.g.* focal therapy). For pulsed laser excitation with $F < 0.8F_{th}$, we could reproducibly generate a consistent pressure output from CNT-PDMS composite films over a long term of >100 hours.

3. Concluding remarks

We demonstrated that the CNT-PDMS composite films offer combined thermal, optical, and mechanical characteristics for high-amplitude ultrasound generation. Extremely fast heat transition of CNT to the surrounding PDMS (~0.4 ns) enables efficient thermo-acoustic generation of ultrasound in a non-ablative regime. Such heat diffusion could be realized in the CNT morphology with a tangled network, not forest, allowing complete infiltration of PDMS among the CNT network down to the substrate surface. This provides a 3-D thermal interface to an individual CNT that is surrounded by the polymer, except the bottom contact with the substrate. Next, as an effective approach to further increase the optical extinction of CNT film, a thin layer of Au (20~30 nm) was deposited through an as-grown CNT network. Formation of the substrate-bound Au could significantly enhance the optical extinction. Finally, mechanical robustness was confirmed by measuring laser damage threshold that determines the maximum-available optical energy for optoacoustic excitation. This revealed that the CNT-PDMS films have an order-of-magnitude higher damage threshold (~477 mJ/cm^2) and optical extinction energy fluence (up to 277 mJ/cm^2) than those of the Cr reference film (48 mJ/cm^2 and 20 mJ/cm^2, respectively). This means that ~14 fold higher optical energy can be used for optoacoustic generation from CNT-PDMS transmitters. Such high degree of robustness against pulsed laser ablation can be attributed to the excellent heat dissipation throughout the composite matrix and the greatly improved adhesion provided by the PDMS to the silica surface. We note that an optoacoustic conversion efficiency of the CNT-PDMS composite is already 1~2 order-of-magnitudes higher than the Cr reference under the same laser fluence [6,14]. For high-amplitude optoacoustic generation, both requirements of efficient energy conversion and robustness are satisfied essentially from the nano-structural characteristics of CNT-PDMS transmitters. This study should be also useful to design and fabricate new nano-composite-based transmitters for diagnostic and therapeutic applications that can be fabricated on a planar or a curved surface.

Experimental Section

Fabrication of CNT-PDMS composite films: For all of the composite films, we used fused silica as substrates for CNT growth. Catalyst layers of 2-nm Fe and 5-nm Al_2O_3 were deposited on the substrates by using a sputtering system. Here, we used slightly thicker catalyst layers, as compared to those of our previous work [6], in order to facilitate the CNT growth. Multi-walled CNTs were grown by using high-temperature chemical vapor deposition in a mixture of C_2H_4/H_2/He (775 °C) [30]. An areal density of CNT films was increased with an exposure time in a high-temperature atmospheric tube furnace. For enhancement of optical extinction, we deposited a 20~30 nm thick Au layer over the as-grown CNT film by using an electron-beam evaporation process. The CNT films with and without the Au layer were then spin-coated with PDMS (2000 r.p.m. for 2 minutes) for composite formation. We used PDMS with a modified chemical composition for high modulus [31] enabling thin-film fabrication (several μm in thickness). The PDMS was cured at 100 °C for 1 hour.

Measurement of optoacoustic pressure waveforms: The pressure waveforms from the CNT-PDMS transmitters were measured by using an optical microring detector that has a broadband frequency response from dc to >100-MHz range under a plane-wave configuration [32–34]. Note that the intrinsic frequency response of the detector is higher and broader than frequency spectra of optoacoustic pressure waveforms. The detection setup allows an acoustic response to duplicate a temporal profile of an incident optical pulse [35], thus accurately quantifying the pulsed peak of pressure waveform without loss in the high-frequency components.

Acknowledgements

This work is supported in part by the NSF Scalable nanomanufacturing program (DMR 1120187) and a subcontract of AFOSR grant FA9550-14-C-0001. H. W. Baac acknowledges the support from the Basic Science Research Program through the National Research Foundation of Korea funded by the Ministry of Education (NRF-2014R1A1A2059612).

Notes and references

[a] School of Electronic and Electrical Engineering, Sungkyunkwan University, Suwon 440-746, Republic of Korea

[b] Department of Mechanical and Automotive Engineering, Seoul National University of Science and Technology, Seoul 139-743, Republic of Korea.

[c] Department of Mechanical Engineering, University of Michigan, Ann Arbor, MI 48109, USA.

[d] Department of Electrical Engineering and Computer Science, University of Michigan, Ann Arbor, MI 48109, USA.

* Corresponding Author: guo@umich.edu.

1 R. J. von Gutfeld and H. F. Budd, Laser-generated MHz elastic waves from metallic-liquid surfaces, Appl. Phys. Lett. 1979, **34**, 617.
2 M. O'Donnell, Y. Hou, J.-S. Kim, S. Ashkenazi, S.-W. Huang, and L. J. Guo, Optoacoustic generation of high frequency sound for 3-D ultrasonic imaging in medicine, Eur. Phys. J. Special Topics 2008, **153**, 53.
3 S. Ashkenazi, Y. Hou, S.-W. Huang, T. Buma, and M. O'Donnell, Photoacoustic Imaging and Spectroscopy, edited by Lihong V. Wang (CRC Press, Boca Raton, 2009), Chap. 18.
4 B. T. Cox and P. C. Beard, Fast calculation of pulsed photoacoustic fields in fluids using *k*-space methods, J. Acoust. Soc. Ame. 2005, **117**, 3616.
5 Y. Hou, J.-S. Kim, S. Ashkenazi, S.-W. Huang, L. J. Guo, and M. O'Donnell, Broadband all-optical ultrasound transducers, Appl. Phys. Lett. 2007, **91**, 073507.
6 H. W. Baac, J. G. Ok, A. Maxwell, K.-T. Lee, Y.-C. Chen, A. J. Hart, Z. Xu, E. Yoon, and L. J. Guo, Carbon-nanotube optoacoustic lens for focused ultrasound generation and high-precision targeted therapy, Sci. Rep. 2012, **2**, 989.
7 H. W. Baac, T. Lee, and L. J. Guo, Micro-ultrasonic cleaving of cell clusters by laser-generated focused ultrasound and its mechanisms, Biomed. Opt. Express 2013, **4**, 1442.
8 H. W. Baac, J. Frampton, J. G. Ok, S. Takayama, and L. J. Guo, Localized micro-scale disruption of cells using laser-generated focused ultrasound, J. Biophoton. 2013, **6**, 905.
9 T. Lee, H. W. Baac, J. G. Ok, H. S. Youn, and L. J. Guo, Controlled generation of single microbubble at solid surfaces by a nanosecond pressure pulse, Phys. Rev. Appl. 2014, **2**, 024007.
10 T. Lee, H. W. Baac, J. G. Ok, H. S. Youn, and L. J. Guo, Nozzle-free liquid microjetting via homogeneous bubble nucleation, Phys. Rev. Appl. 2015, **3**, 044007.
11 E. Biagi, F. Margheri, and D. Menichelli, Efficient laser-ultrasound generation by using heavily absorbing films as targets, IEEE Trans. Ultrason. Ferroelectr. Freq. Control 2001, **48**(6), 1669.
12 T. Buma, M. Spisar, and M. O'Donnell, High-frequency ultrasound array element using thermoelastic expansion in an elastomeric film, Appl. Phys. Lett. 2001, **79**, 548.
13 Y. Hou, J.-S. Kim, S. Ashkenazi, M. O'Donnell, and L. J. Guo, Optical generation of high frequency ultrasound using two-dimensional gold nanostructure, Appl. Phys. Lett. 2006, **89**, 093901.
14 H. W. Baac, J. G. Ok, H. J. Park, T. Ling, S.-L. Chen, A. J. Hart, and L. J. Guo, Carbon nanotube composite optoacoustic transmitters for strong and high frequency ultrasound generation, Appl. Phys. Lett. 2010, **97**, 234104.
15 R. J. Colchester, C. A. Mosse, D. S. Bhachu, J. C. Bear, C. J. Carmalt, I. P. Parkin, B. E. Treeby, I. Papakonstantinou, and A. E. Desjardins, Laser-generated ultrasound with optical fibres using functionalised carbon nanotube composite coatings, Appl. Phys. Lett. 2014, **104**, 173502.
16 B.-Y. Hsieh, J. Kim, J. Zhu, S. Li, X. Zhang, and X. Jiang, A laser ultrasound transducer using carbon nanofibers-polydimethylsiloxane composite thin film, Appl. Phys. Lett. 2015, **106**, 021902.
17 S. H. Lee, Y. Lee, and J. J. Yoh, Reduced graphene oxide coated polydimethylsiloxane film as an optoacoustic transmitter for high pressure and high frequency ultrasound generation, Appl. Phys. Lett. 2015, **106**, 081911.
18 Y. Guo, H. W. Baac, S. L. Chen, T. B. Norris, and L. J. Guo, Broad-band, high-efficiency optoacoustic generation using a novel photonic crystal-metallic structure, Proc. SPIE 2011, **7899**, 78992C.
19 D. S. Kopylova, I. M. Pelivanov, N. B. Podymova, and A. A. Karabutov, Acoust. Phys. 2008, **54**, 783.
20 I. M. Pelivanov, D. S. Kopylova, N. B. Podymova, and A. A. Karabutov, Optoacoustic technique for thickness measurement of submicron metal coatings, Laser Phys. 2009, **19**(6), 1350.
21 H.-F. Shi, J. G. Ok, H. W. Baac, and L. J. Guo, Low density carbon nanotube forest as an index-matched and near perfect absorption coating, Appl. Phys. Lett. 2011, **99**, 211103.
22 M. F. L. De Volder, S. H. Tawfick, R. H. Baughman, and A. J. Hart, Carbon nanotubes: present and future commercial applications, Science 2013, **339**, 535.
23 A. L. McKenzie, Physics of thermal processes in laser-tissue interaction, Phys. Med. Biol. 1990, **35**(9), 1175.
24 A. A. Oraevsky, Photoacoustic Imaging and Spectroscopy, edited by Lihong V. Wang (CRC Press, Boca Raton, 2009), Chap. 30.
25 R. S. C. Cobbold, Foundations of Biomedical Ultrasound (Oxford University Press, New York, 2007), Chap. 6.
26 V. E. Gusev and A. A. Karabutov, Laser Optoacoustics (American Institute of Physics, New York, 1993), Chap. 2.
27 Y. C. Choi, D. W. Kim, T. J. Lee, C. J. Lee, and Y. H. Lee, Growth mechanism of vertically aligned carbon nanotubes on silicon substrates, Synth. Met. 2001, **117**, 81.
28 K. Mizuno, J. Ishii, H. Kishida, Y. Hayamizu, S. Yasuda, D. N. Futaba, M. Yumura, and K. Hata, A black body absorber from vertically aligned single-walled carbon nanotubes, Proc. Natl Acad. Sci. USA 2009, **106**(15), 6044.
29 X. J. Wang, J. D. Flicker, B. J. Lee, W. J. Ready, and Z. M. Zhang, Visible and near-infrared radiative properties of vertically aligned multi-walled carbon nanotubes, Nanotechnology 2009, **20**(21), 215704.
30 A. J. Hart and A. H. Slocum, Rapid growth and flow-mediated nucleation of millimeter-scale aligned carbon nanotube structures from a thin-film catalyst, J. Phys. Chem. B 2006, **110**, 8250.
31 C. Pina-Hernandez, J.-S. Kim, L. J. Guo, and P.-F. Fu, High-throughput and etch-selective nanoimprinting and stamping based on fast-thermal-curing poly(dimethylsiloxane)s, Adv. Mater. 2007, **19**, 1222.
32 C.-Y. Chao, S. Ashkenazi, S.-W. Huang, M. O'Donnell, and L. J. Guo, High-frequency ultrasound sensors using polymer microring resonators, IEEE Trans. Ultrason. Ferroelectr. Freq. Control 2007, **54**(5), 957.
33 H. W. Baac, T. Ling, H. J. Park, and L. J. Guo, Evaluation of optoacoustic conversion efficiency of light-absorbing films for optoacoustic transmitter applications, Proc. SPIE 2011, **7899**, 789940.
34 C. Zhang, T. Ling, S.-L. Chen, and L. J. Guo, Ultrabroad bandwidth and highly sensitive optical ultrasonic detector for photoacoustic imaging, ACS Photonics 2014, **1**(11), 1093.
35 G. J. Diebold, T. Sun, and M. I. Khan, Photoacoustic monopole radiation in one, two, and three dimensions, Phys. Rev. Lett. 1991, **67**, 3384.

